The DNA damage response relies on the characteristics of ionizing particles in myogenic cells

Haser Hasan Sutcu[1#*], Arthur Thomas--Joyeux[1], Mikaël Cardot-Martin[2], François Vianna[2], Mohamed Amine Benadjaoud[3], Marc Benderitter[4], Céline Baldeyron[1*]

[1] Institut de Radioprotection et de Sûreté Nucléaire (IRSN), PSE-SANTE/SERAMED/LRAcc, F-92260, Fontenay-aux-Roses, France

[2] Institut de Radioprotection et de Sûreté Nucléaire (IRSN), PSE-SANTE/SDOS/LMDN, F-13115, Saint-Paul-Lez-Durance, France

[3] Institut de Radioprotection et de Sûreté Nucléaire (IRSN), PSE-SANTE/SERAMED, F-92260, Fontenay-aux-Roses, France

[4] Institut de Radioprotection et de Sûreté Nucléaire (IRSN), PSE-SANTE, F-92260, Fontenay-aux-Roses, France

[#] Present address: Université Paris Cité, Inserm, CEA, Stabilité Génétique Cellules Souches et Radiations/iRCM, F-92265, Fontenay-aux-Roses, France; Université Paris-Saclay, Inserm, CEA, Stabilité Génétique Cellules Souches et Radiations/iRCM, F-92265, Fontenay-aux-Roses, France

* Co-corresponding authors: Céline Baldeyron, celine.baldeyron@irsn.fr; Haser Hasan Sutcu, haser.sutcu@cea.fr

Keywords: Skeletal muscle cells, non-homologous end-joining, homologous recombination, ionizing particle, microbeam irradiation

Summary

Mouse skeletal muscle cells and their precursor cells irradiated by ion microbeam show DNA damage response and DNA repair dynamics that vary according to the characteristics of ionizing particles delivered.

Graphical Abstract

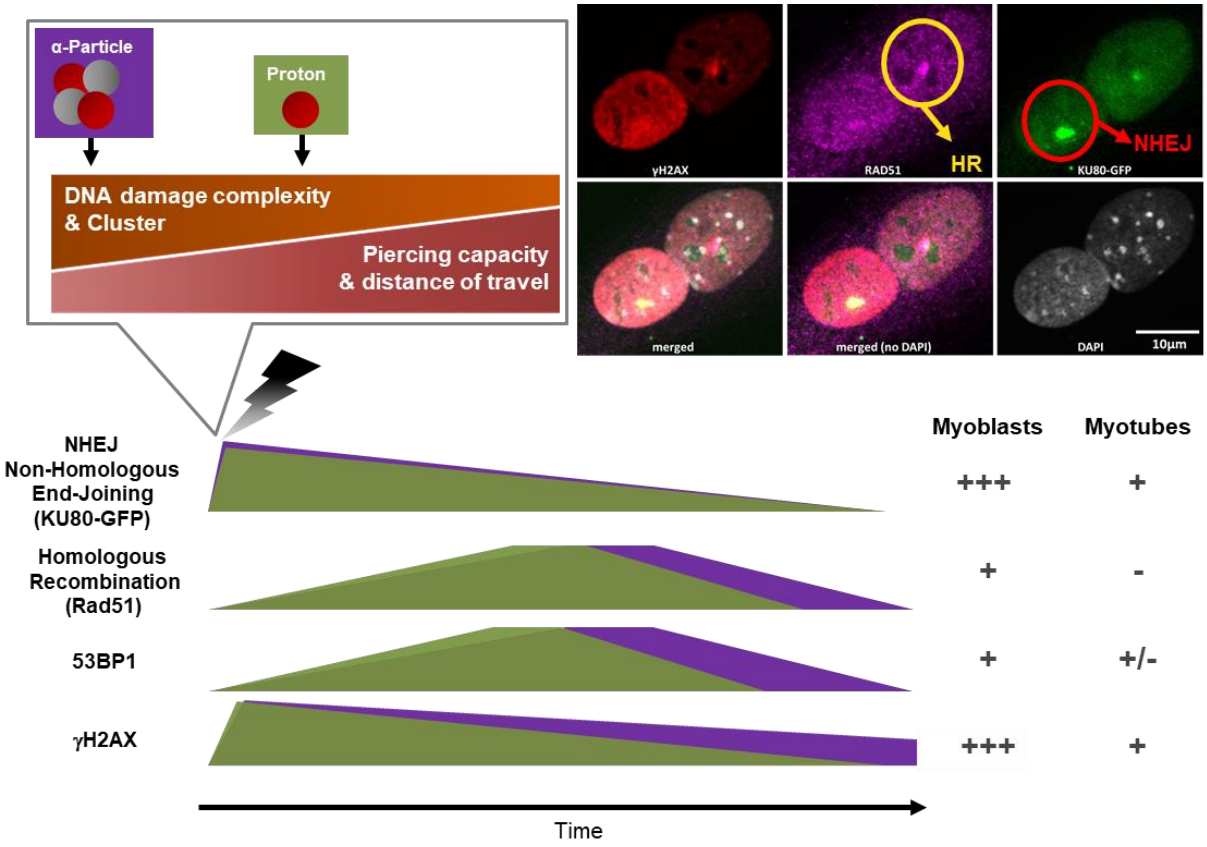

Abstract

DNA integrity and stability are vital for proper cellular activity. Nevertheless, to treat cancer patients, DNA is the main target for inducing tumoral cell death. Nowadays, cancer treatment is improving by the development of new technologies, protocols and strategies. Amongst them, the introduction of charged particles as a form of radiotherapy is underway. However, tumor-neighboring healthy tissues are still exposed to ionizing radiations (IR) and subject to late side effects. Skeletal muscle is one of those tissues most likely to be affected. To decipher the DNA damage response (DDR) of skeletal muscle cells, myogenic cells, we irradiated them with microbeams of protons or α-particles and followed the accumulation of DDR proteins at irradiation sites. Thereby, we showed that myoblasts, proliferating myogenic cells, repair IR-induced DNA damage through both non-homologous end-joining and homologous recombination with different recruitment dynamics depending on the characteristics of ionizing particles (type, energy deposition and time after irradiation), whereas myotubes, post-mitotic myogenic cells, display reduced DNA damage response.

Introduction

The most common cancer treatments are surgical removal, chemotherapy and radiotherapy, alone or combined depending on the type, grade and localization of cancer (1). Although the purpose of these therapies is to get rid of cancerous cells, the therapies themselves give rise to undesired side effects. During radiotherapy, DNA is considered as the main cellular target for biological effects of ionizing radiation (IR) (2,3). IR produces a wide spectrum of DNA lesions, among which DNA double-strand breaks (DSBs) play a key role in the induction of cell cycle arrest and cell death. Indeed, DSBs are considered to be the most deleterious DNA lesions for genome integrity and stability (4). DSBs can be repaired by four distinct repair pathways in eukaryotic cells: classical non-homologous end-joining (c-NHEJ or NHEJ), homologous recombination (HR), single-strand annealing (SSA), and alternative non-homologous end-joining (alt-NHEJ) (4,5). However, NHEJ and HR are the two major mechanisms used for the repair of DSBs, while SSA and alt-NHEJ process the residual DSBs that could not be repaired by NHEJ and HR. While NHEJ is known to be active during the entire cell cycle, HR is limited to S-G2 phases, as it requires template DNA for resynthesis of damaged region guided by homologous sequences on the sister chromatid (6). The principal repair pathway of IR-induced DSBs is reported to be NHEJ (6), which proceeds through KU70/KU80 heterodimer recruitment and formation of DNA-PK complex with DNA-PKcs (DNA-PK catalytic subunit), initiating DNA end-processing, followed by bringing processed DNA broken ends together and ligating by DNA Ligase IV with its cofactors, XRCC4 and XLF/Cernunnos (7,8). Despite this, the radiosensitivity of cells with deficiency in HR-mediated DSB repair (9-11) suggests that HR could also be implicated in the repair of DNA damage induced by low or high linear energy transfer (LET) particles.

Nowadays, along with new technologies, new protocols and modalities of radiotherapy are introduced for preclinical studies and clinical use. Depending on the type and/or invasiveness of cancer to be treated, radiotherapy options range from photon (X-ray, gamma ray)- to charged particle (proton, carbon)-treatments, whether with fractionated (12,13), ablative (14), or flash (15) doses. Today, the 5-year survival rate is 70 % and above for certain types of cancer (e.g. prostate cancer, non-Hodgkin lymphoma, kidney and renal pelvis cancer, ovary cancer, breast cancer) (16). Consequently, along with increased survival rate, late onset side effects of cancer therapies can be seen (17,18). Accordingly, skeletal muscle (i.e., myofibers), which makes up to approximately 40 % of the body mass (19), is one of the most liable organs to be exposed to IR as an adjacent healthy tissue during radiotherapy. Despite that skeletal muscle tissue is considered to be radioresistant (20-22), many studies show that, in long term, muscle surrounding the radiotherapy target displays physiological sequelae depending on the dose, frequency, or quality of IR (23,24). Such muscular problems developed upon radiotherapy include muscle wasting, cachexia, contractures, malfunctioning and weakness, and affect the life quality of patient. Moreover, these complications are even more severe for the juvenile patients who are still under development (20,25,26). Although these side effects could be attenuated by lifestyle, exercise and diet (24,27), their causes at the molecular and mechanistic levels are still poorly understood.

Skeletal muscle cells originate from unipotent muscle stem cells (28). In developing juvenile organisms muscle stem cells are mostly active and proliferative to contribute for skeletal muscle growth (29), whereas in adults, they are quiescent and are called satellite cells (SCs), since they are located at the periphery of myofibers between the basal lamina and the sarcolemma. The SCs only activate for self-renewal, muscle homeostasis and regeneration (30,31). Thus, it is only upon activation that SCs proliferate in the form of myoblast, differentiate and fuse into multi-nucleated myotubes and mature into myofibers (31). In order to increase our knowledge of late-onset consequences of radiotherapy on muscle, it is therefore important to assess the efficiency of DNA damage repair mechanisms specific to multi-nucleated myofibers as well as its mono-nuclear precursors cells. This could also give a better understanding for the greater impact of radiotherapies observed on juvenile patients, in which the muscle precursors are still active, unlike in adults. Previously, it has been reported that adult muscle stem cells have more efficient and accurate DNA repair capacity than their committed progeny (32). Recently, we have also shown that multi-nucleated skeletal myofibers, generated from muscle stem cells of neonatal mice or immortalized myoblasts, have a reduced DNA damage response (DDR) in comparison to their precursors, myoblasts upon x-ray or α-particle irradiation (33). Additionally, our previous findings suggest that repair of DSBs induced either by x-ray or α-particle irradiation in mono

and multinuclear myogenic cells is essentially carried out by NHEJ (33) as in their progenitor, muscle stem cells (32,34).

Due to the increasing, though still marginal, use of protons (proton therapy) and alpha emitters (nuclear medicine), and based on our recent findings on the DNA damage response in myogenic cells upon α-particle irradiation, we performed a study of the DDR in myogenic cells according to the type and characteristics of ionizing particles delivered and the energy deposited. Therefore, taking advantage of ion microbeam technology (35), we delivered different numbers of 4 MeV protons and 6 MeV α-particles to induce local DNA damage at the sub-nuclear level within nuclei of myogenic cells and we followed the recruitment kinetics of some DDR proteins coupled to GFP throughout myogenic differentiation. Thereby, we demonstrated that DSB repair (DSBR) mechanisms in proliferating myogenic cells, myoblasts, switch as a function of energy deposition and time after irradiation, whatever the particle delivered, proton or α-particle. Additionally, we found that myoblasts orchestrate IR-induced DSB repair with dynamics that depend on the type of high LET particle used, proton or α-particle, while differentiated myotubes remained with declined DNA damage response as was previously reported (33).

Materials and methods

Myogenic cell culture

Immortalized myogenic cells, C2C7 were kindly gifted by Miria Ricchetti (Institut Pasteur, Département de Biologie du Développement et Cellules Souches, Laboratoire de Mécanismes Moléculaires du Vieillissement Pathologique et Physiologique, Paris, France). We maintained the C2C7 cells (36) in myoblast state (proliferative state), by culturing in growth medium (GM) based on DMEM Glutamax (Gibco) supplemented with 20 % fetal calf serum (FCS, Eurobio), and 100 $U.mL^{-1}$ penicillin and 100 $\mu g.mL^{-1}$ streptomycin (i.e., 1 % P/S; Gibco). To generate post-mitotic myotubes, once myoblasts have reached 80 % confluency, we switched the medium to differentiation medium (DM) corresponding to phenol-red free DMEM (Gibco) complemented with 2 % horse serum (HS, Gibco), 1 % P/S, 1% Glutamax (Gibco), and 1% Sodium Pyruvate (Gibco). To note, 50 % of DM was refreshed after 3 days and every consecutive day after. We incubated all the cells in a humidified atmosphere at 37 °C with 5 % CO_2 and 3 % O_2.

During irradiation experiments on MIRCOM platform, we grew myoblasts and generated myotubes on 4 µm thick polypropylene foil (Goodfellow) pre-coated with 10 $ng.\mu L^{-1}$ of Cell-Tak (Corning) followed by 10 % Matrigel (Corning) in DMEM on special PEEK dishes, as described in (37). On the day of irradiation, we replaced the GM medium with phenol-red free version to reduce potential autofluorescence.

Plasmids and transfections

The plasmids expressing GFP-tagged protein of interest were kindly provided by Pascale Bertrand (53BP1-GFP; CEA, iRCM/IBFJ, UMRE008 Stabilité Génétique, Cellules Souches et Radiations, Fontenay-aux-Roses, France), Dik C. van Gent (KU80-GFP; Erasmus MC, Departments of Cell Biology and Genetics, Rotterdam, The Netherlands), and G. Almouzni (HP1α-GFP; Institut Curie, UMR3664 Dynamique du Noyau, Paris, France). These plasmids were transfected in C2C7 myoblasts with TurboFect (ThermoFisher Scientific) according to the manufacturer's instructions. To get successful transfection, C2C7 cells were transfected 1-day post-seeding at about 50 % - 60 % confluency. To obtain stable and homogenous GFP-tagged protein expressing C2C7 lines, 24 h post-transfection the GFP-expressing cells were enriched under $1mg.mL^{-1}$ of geneticin (G418 sulfate; Gibco) selection for 10 consecutive days. Then, the GFP-tagged protein expressing C2C7 cells were isolated by FACs sorting and further expanded (33).

MIRCOM, Microbeam particle irradiation

We performed the localized irradiation of samples by 4 MeV protons, or 6 MeV α-particles generated from hydrogen and helium ions, respectively, by using the MIRCOM facility, operated by the Institute for Radiological Protection and Nuclear Safety (IRSN) in Cadarache, France (38). This facility is equipped with a focused ion microbeam, which is produced by a 2 MV Tandetron™ accelerator manufactured by High Voltage Engineering Europa B.V. (HVEE, Amersfoort, The Netherlands). It has been designed to

perform in-air targeted micro-irradiation of living biological samples with a controlled number of ions and a targeting accuracy of 2.1 ± 0.7 µm with a beam spot diameter of a few micrometers (38).

As protons and α-particles have low penetration capacity and thus short travel distance through matter, the cells are seeded in a specific PEEK cell dish with a 4 µm thick polypropylene foil (Goodfellow) (37). The LET of the particles at the entrance of the samples after going through the extraction window (150 nm), a residual air layer (250 µm), and the polypropylene foil (4 µm) is 84 keV.µm^{-1} for 6 MeV α-particles (39) and 10 keV.µm^{-1} for 4 MeV protons, calculated with SRIM (38,40). Thus, the specific energy deposited within the targeted volume is approximately 1 mGy for one 4 MeV proton and 1 cGy for one 6 MeV α-particle in these experimental conditions of localized irradiation.

During irradiation, cells are placed under an inverted epifluorescence microscope (AxioObserver™ Z1, Carl Zeiss Microscopy GmbH, Jena, Germany) within a 37 °C heating chamber. The relevant nuclei of GFP-expressing cells are identified and selected for irradiation with a 20x objective (Zeiss LD Plan-NEOFLUAR 20x/0.4 Korr). Then, we targeted the nuclei of selected cells with the indicated number of protons or α-particles, which was determined by the definition of an opening time of the microbeam on each target, as described previously (33,38,39). Thus, the energy deposition of each irradiation with protons or α-particles is directly correlated to the number of particles delivered.

To follow the recruitment kinetics of our GFP-tagged proteins of interest, we started time-lapse imaging 10 s before targeted irradiation with the indicated number of particles and recorded images every 2 s with a monochromatic AxioCam™ MRm rev. 3 CCD camera (Carl Zeiss Microscopy GmbH, Germany) using the CRionScan software (38). We recorded images with an exposure time of 800 ms. In total, we kept cells in the microbeam chamber for less than 30 min.

Immunostaining and image acquisition

At the indicated time following irradiation, the cells were fixed with 2 % paraformaldehyde (PFA; EMS, Euromedex) in phosphate-buffered saline (PBS; Gibco) for 20 min, and then permeabilized with 0.5 % Triton X-100 (Sigma-Aldrich) in PBS for 5 min. To increase the stringency cells were washed with 0.1% Tween 20 (Sigma-Aldrich) in PBS (PBS-T) for 20 min, then blocked with 5% BSA (Sigma-Aldrich) in PBS-T. Next, the cells were incubated with the indicated primary antibodies overnight at 4°C. After three washes in PBS-T, the cells were incubated with the appropriate fluorophore-conjugated secondary antibodies for 1 h at room temperature (RT). After three washes in PBS-T, the cells were incubated with 0.5 µg/mL DAPI (Molecular Probes) in PBS for 5 min at RT. Finally, after three washes in PBS, cells on polypropylene foil were mounted between slide and coverslip with Prolong Diamond antifade mounting medium (Molecular Probes). The cells were imaged with C-Plan Apochromat 63x/1.4 Oil DIC M27 objective under a LSM 780 NLO confocal microscope, piloted with the Zen Black 2011 SP4 software (Carl Zeiss MicroImaging GmbH, Germany).

Antibodies

Primary antibodies used during immunofluorescence experiments are: rabbit anti- 53BP1 (Bio-Techne, Novus Biologicals, NB 100-304; 1:500); mouse anti-γH2AX (Millipore, UpState, 05-636; 1:2,000); rabbit anti-RAD51 (Abcam, ab137323; 1:400).

Secondary antibodies used are: donkey anti-mouse or donkey anti-rabbit coupled to Alexa Fluor 594 or 647 (Invitrogen, ThermoFisher Scientific; 1:1,000). To amplify the GFP fluorescence intensity post-fixation, we used GFP booster nanobodies conjugated with Alexa fluor 488 (Chromotek, gb2AF488; 1:500).

Quantification and Statistical analysis

All the images were processed, analyzed, and quantified by ImageJ software (version 1.53e) (41), and statistical analyses were performed by Prism software (version 9; GraphPad Inc.) and Excel (Microsoft).

In order to quantify the fluorescence re-localization of GFP-tagged proteins observed by time-lapse imaging upon MIRCOM irradiation, we manually selected and followed regions of interest (ROI). We measured the mean intensity of ROIs in every image and plotted them against time. To obtain the relative intensity of GFP-tagged repair proteins recruited at the irradiation site, the mean intensity of non-

irradiated site was subtracted from ROIs and normalized to mean fluorescence intensity of total nuclei. Then the obtained data were corrected for non-specific fluorescence bleaching and normalized for the fluorescence intensity measured before irradiation. All statistical analyses were performed from at least 3 independent experiments. The smoothing and comparison between the kinetic curves of KU80-GFP and 53BP1-GFP recruitment under different irradiation conditions were performed within the generalized additive models (GAM) framework (42) where the smoothing of the KU80-GFP time-kinetic data was performed using penalized splines. The statistical inference on the difference between two kinetic curves was based on the uncertainties of the smoothing process: a difference at a given time-point was considered as significant if its associated confidence interval did not contain zero. This approach permitted us to highlight the significant differences along the time-point values.

In order to investigate the impact of the experimental conditions on each monocellular fluorescence intensities, we performed a partial least squares discriminant analysis (PLS-DA) on the monocellular RAD51, γH2AX and GFP-KU80 signals for the classification of groups defined by their type and number of particles as well as their time points post irradiation. The PLS-DA is a supervised dimension approach aiming to project a given dataset (here the fluorescence intensity matrices) on a subspace optimally separated according to a categorical variable (here the experimental conditions). Similarly, to its unsupervised dimension reduction counterpart, the well-known principal component analysis (PCA), the interpretation of PLS-DA consists on examining the contribution of the original covariates in the construction of its dimension components (called loadings).

Results

The dynamic behavior of KU80-GFP at the DNA damage site depends on the type and number of particles delivered.

To assess initial IR-induced DNA damage response of myogenic cells, we used the immortalized murine C2C7 cells stably expressing GFP-tagged repair proteins and the microbeam MIRCOM facility, which allows *in situ* localized irradiation within the nuclei of living cells (33,39,43). The MIRCOM microbeam can deliver a controlled number of a given particle. Here, we targeted either 1,000; 200 or 50 α-particles, or 10,000; 2,500 and 500 protons in order to have comparable deposited energy between these two types of particles at the localized irradiation sites (see Materials and methods). Since KU80 in heterodimer with KU70 plays a crucial role as a DNA damage sensor, followed by forming the essential DNA-PK complex to initiate DSBR mediated by NHEJ (7,44), we first monitored the accumulation of KU80-GFP protein at the locally irradiated zones over a time frame of 5 min in myoblasts (Fig. 1, A-B) and myotubes (Fig. S1, A-B).

First, we found that in KU80-GFP-expressing C2C7 cells at the myoblast state, the recruitment of KU80-GFP to DNA damage sites shows similar kinetics upon localized irradiation with 1,000 α-particles (Fig. 1, C) or 10,000 protons (Fig. 1, D). Immediately after irradiation by 1,000 α-particles or 10,000 protons, KU80-GFP accumulated at the sites of DNA damage, reaching a maximum level of recruitment within 60 s followed by its gradual release (Fig. 1, C-D). In contrast, in KU80-GFP-expressing C2C7 cells at the myotube state, we found reduced recruitment of KU80-GFP at the sites of DNA damage induced by a 1,000 α-particles irradiation in comparison to myoblasts (Fig. 1, A and C vs Fig. S1, A and C), as we previously reported (33). Likewise, we observed that this was also the case upon 10,000 protons irradiation (Fig. 1, B and D vs Fig. S1, B and D), albeit to a lesser extent.

Then, by reducing the number of particles delivered (i.e., 200 and 50 α-particles or 2,500 and 500 protons), we observed a decrease in the accumulation of KU80-GFP in myoblasts at localized irradiation sites (Fig 1, C-D) transiently reaching to plateau earlier, followed by its almost immediate release in comparison to irradiations with highest number of particles (i.e., 1,000 α-particles and 10,000 protons). Furthermore, we could observe minor but statistically significant differences in the recruitment kinetics of KU80-GFP according to the number of particles delivered, in particular upon α-particle irradiation (Fig. 1 C-D). In similar fashion, along with number of α-particles (Fig. S1, A and C) and protons (Fig. S1, B and D) delivered, KU80-GFP recruitment in myotubes reduces. Despite lower KU80-GFP accumulation than in myoblasts, whatever the nature and number of particles delivered, KU80-GFP is retained longer at irradiation sites in myotubes (Fig. S1, C and D), and especially upon targeted proton irradiation (Fig. S1, D).

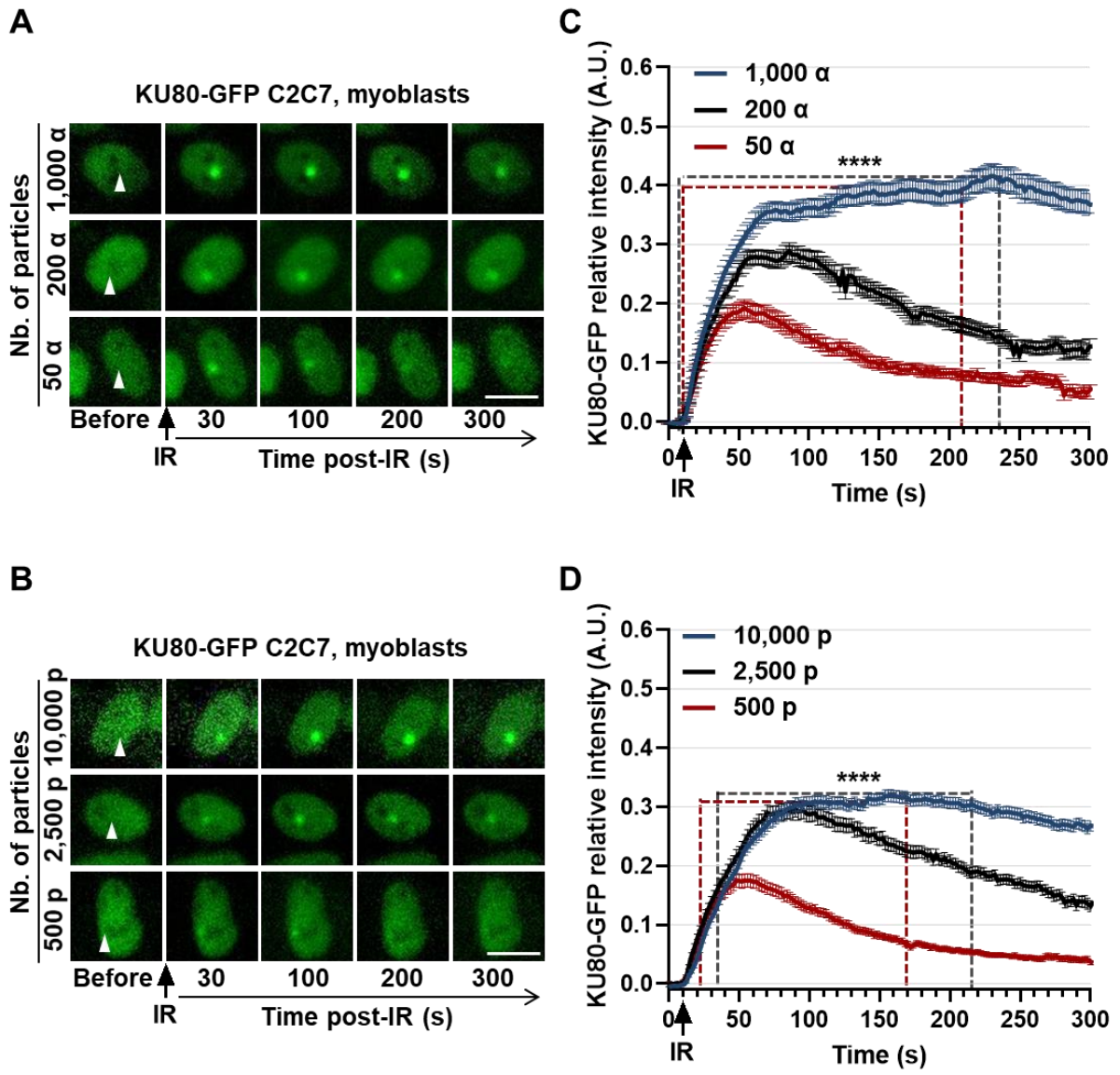

Figure 1 : Recruitment kinetics of NHEJ factor KU80-GFP to the site of localized α-particle and proton irradiation within nuclei of proliferating myoblasts. *Myoblast nuclei were irradiated at a defined single spot by delivering the indicated number of charged ions. The response of GFP-tagged proteins upon localized irradiation was followed by live cell imaging every 2 seconds on an epifluorescence Zeiss microscope. The irradiation was applied after the first 5 images.* ***(A, B)*** *Representative images of KU80-GFP recruitment in stably KU80-GFP-expressing C2C7 myoblasts upon localized irradiation with reducing particle number of α-particles (A) and protons (B). The local irradiation site is marked with white arrowhead. Scale bar represents 10µm.* ***(C, D)*** *Kinetic curves of KU80-GFP recruitment obtained from A and B upon local irradiation with reducing number of α-particles (C) and protons (D) delivered. Error bars represent the SEM obtained from N= 3 independent experiments with 65 - 210 nuclei / condition analyzed in C and 42 - 175 nuclei / condition analyzed in D. Statistical analysis performed by using generalized additive models (GAM) framework model and comparing each time point. Dashed boxes represents the region of slopes with significant difference between the kinetic curves. Color code of boxes represents the same color kinetic curve vs curve of highest number of particle irradiation. **** p< 0.00001.*

Together, our results suggest that in myogenic cells the accumulation and disappearance of KU80-GFP proteins at localized irradiation sites are correlated with the number of particles delivered during irradiation, thereby with the deposited energy and thus potentially with the number, complexity and

clustering of DNA lesions induced. Indeed, in myoblasts, the faster disappearance of KU80-GFP upon low number of particle irradiation compared to the one with high number of particles could correlate with amount of induced DNA damage and with fast DSB repair component. On the contrary, in myotubes, reduced but persisting accumulation of KU80-GFP, which was previously reported to be with high turn-over of KU80 proteins at DNA damage sites (33), suggests an insufficient amount of KU80 retained at damaged DNA to process the DNA lesions despite its recruitment to the irradiation site. Additionally, absence of other repair pathways; notably HR and declined BER, as demonstrated in (33), myotubes may have globally weaker DDR than myoblasts, consequently affecting and delaying KU80 dependent DSBR.

The accumulation rate of 53BP1-GFP at DNA damage sites is inversely proportional to the number of particles delivered.

53BP1 is a key protein mediating the signaling of DSBs and orchestrating the choice of DSBR pathways (45). Indeed, 53BP1 has a competitive role with BRCA1, a central HR factor, by inhibiting DNA end-resection, and thus favoring NHEJ (46). To assess the initial response of 53BP1 to irradiation, we induced local DNA damage by microbeam irradiation within stably 53BP1-GFP-expressing C2C7 cells and monitored its recruitment to micro-irradiation sites in the time frame of 5 min (Fig. 2, A-B).

As we have recently shown that there is almost no initial response of 53BP1 in myotubes upon 1,000 α-particles irradiation (33), here we demonstrated that this is also the case with a dose of 10,000 protons (Fig. S2, A and C). Surprisingly, a dose of 50 α-particles triggered a small but significant increase in the initial 53BP1-GFP recruitment to local IR-induced DNA damage sites in myotubes (Fig. S2, A). Even more remarkably, we found in myoblasts that lowering the number of particles to 50 α-particles or to 500 protons induces a recruitment of 53BP1-GFP to irradiation sites almost 2-fold bigger than that induced by 1,000 α-particles or 10,000 protons within 5 min (Fig. 2, A-B). Unlike KU80-GFP, 53BP1-GFP in myoblasts continues to accumulate and does not reach a plateau in this time-frame (Fig. 2 vs Fig. 1).

To follow the recruitment of endogenous 53BP1 protein beyond the first five minutes to IR-induced DNA damage sites and compare its kinetics to that of KU80, we immuno-labelled KU80-GFP-expressing cells with antibodies against 53BP1 and the phosphorylated form of the histone variant H2AX (known as γH2AX), used as a DSB biomarker (47) and analyzed their fluorescence intensity. We thus confirmed in KU80-GFP-expressing myoblasts locally irradiated with 1,000 α-particles or 10,000 protons that 53BP1 recruitment continues to increase at the IR-induced DNA damage sites up to 6 h post-irradiation (Fig. 2, C-D), while KU80-GFP and γH2AX signals gradually disappear over time (Fig. 2, C). In addition, 1h post-irradiation we found that myoblasts irradiated by 10,000 protons have a higher signal of 53BP1 at irradiation sites than those irradiated by 1,000 α-particles (Fig. 2, D). Decreasing the number of α-particle or proton does not seem to reduce the 53BP1 signal detected at irradiation sites 1 h post-irradiation (Fig. 2, E-F), in contrast to the diminishing KU80-GFP and γH2AX signals which correlate with the number of particles used for irradiation (Fig. 2, E) and in line with our above-mentioned kinetics data for KU80-GFP (Fig. 1). Moreover, at 6 h post-irradiation α-particle-irradiated myoblasts show significantly higher 53BP1 intensity at irradiation sites than those irradiated by protons (Fig. 2, C). These results suggest faster signaling and/or repair of proton-irradiation-induced DNA damage in myoblasts than those induced by α-particle-irradiation.

In contrast, myotubes show a delayed and reduced 53BP1 recruitment to irradiated sites up to 6 h post-irradiation. Moreover, differentiating mono-nuclear cells, designated as myocytes, present an intermediate profile (Fig. S2, B-C vs Fig. 2, D). These results indicate that 53BP1 recruitment to IR-induced DNA lesions is progressively reduced along the myogenic differentiation, reinforcing our recent data (33).

Taken together, our data show that in myoblasts low particle number induces faster 53BP1 recruitment to localized irradiation sites than high particle number during the initial DDR. Then, at 1 h post-irradiation the accumulation of 53BP1 at damaged DNA site is similar, regardless of the number of particles used. Finally, in myoblasts the release of 53BP1 from DNA damage site is faster upon proton-irradiation than upon α-particle-irradiation when the highest numbers of particles are delivered (1,000 α-particles vs 10,000 protons).

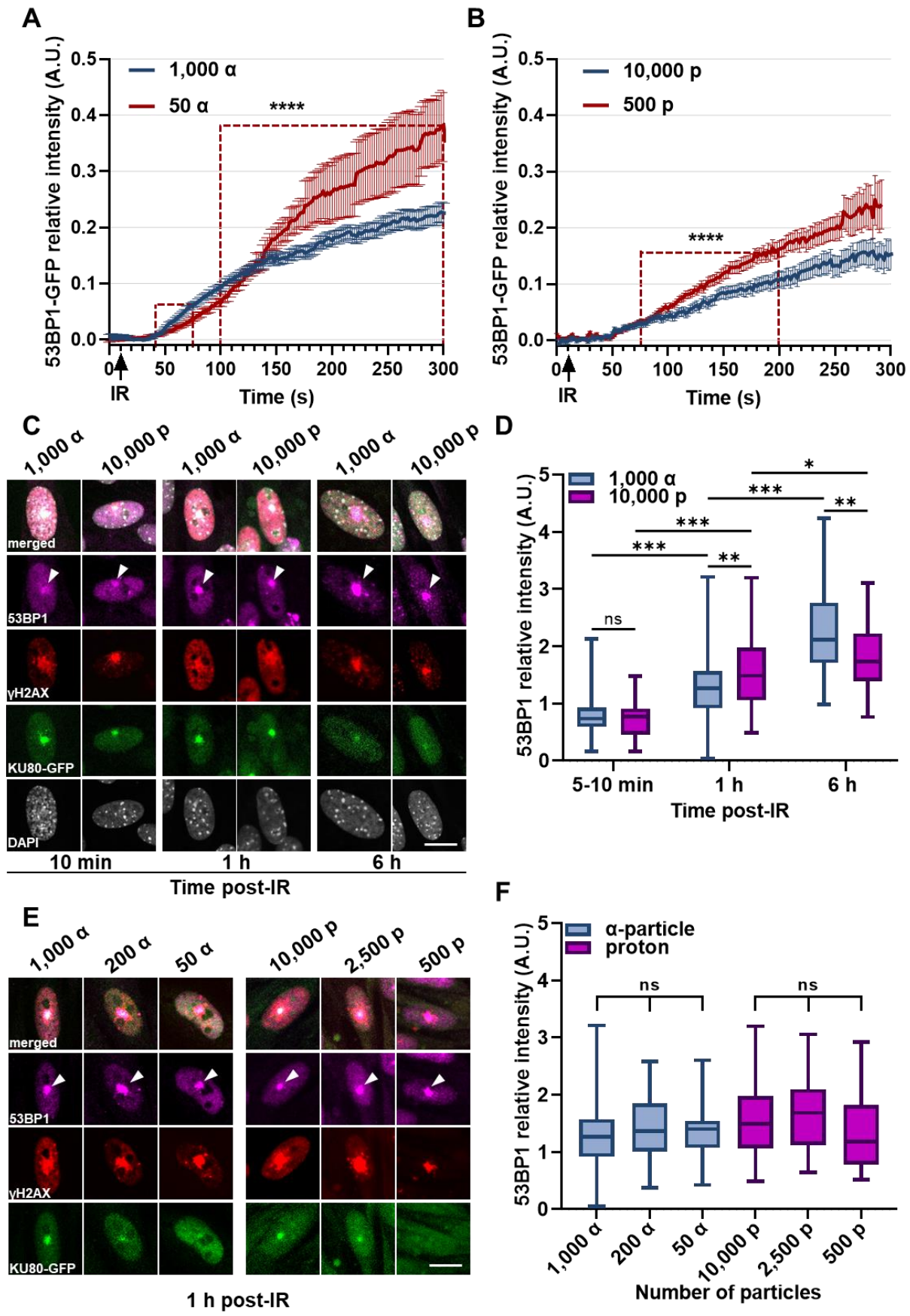

Figure 2: Response of DDR protein 53BP1 upon localized α-particle and proton irradiation within nuclei of myoblasts. (A, B) *Kinetic curves of 53BP1-GFP recruitment in stably 53BP1-GFP-expressing C2C7 myoblasts upon 1,000 and 50 α-particles irradiation (A), or upon 10,000 and 500 protons*

*irradiation (B). N= 3 independent experiments, mean ± SEM from 71 – 109 nuclei / condition analyzed in (A) and 23 - 32 nuclei / condition analyzed in (B). Statistical analysis performed by using GAM framework model and comparing each time point. Dashed boxes represent the region of slopes with significant difference between the kinetic curves. Color code of boxes represents the same color kinetic curve vs curve of highest number of particle irradiation. **** p< 0.00001.* ***(C, E)*** *Representative images of stably KU80-GFP-expressing proliferative C2C7 myoblasts immunostained with antibodies against 53BP1 and the phosphorylated form of the histone variant H2AX (γH2AX) at the indicated time-points after localized 1,000 α-particles and 10,000 protons irradiation (C), and 1h after localized irradiation by 1,000, 200 and 50 α-particles or by 10,000, 2,500 and 500 protons (E). DNA is counterstained with DAPI, local irradiation site marked with white arrowhead and scale bar, 10 µm.* ***(D, F)*** *Relative fluorescence intensities of 53BP1 staining at local irradiation sites within nuclei of cells from (C) shown in (D) and from (E) shown in (F). N= 3 independent experiments with 22 - 94 nuclei / condition analyzed in (D) and 31 - 94 nuclei / condition analyzed in (F). Data are presented in box-plots, with boxes representing the median with upper and lower quartiles and whiskers representing the min and max values. Statistical significance is obtained by 1-way ANOVA with post-hoc Tukey's multiple comparison test. p-value are ns p> 0,05, * p< 0.05, ** p< 0.01, *** p< 0.001.*

NHEJ and HR balance in the processing of ionizing particle-induced DSBs in myoblasts.

Our above-mentioned results show that the early 53BP1 recruitment to damaged DNA site is inversely correlated with the number of particles delivered. As 53BP1 plays a major role in the choice of DSBR pathways (46), we next investigated the dynamic behavior of both NHEJ and HR key factors upon localized charged particle irradiation only in myoblasts, as myotubes have no HR activity (33). During HR, RAD51 plays a central role forming the nucleoprotein filament over the generated 3' ssDNA at DSB ends (48), which is required for the homology search and invasion of template duplex DNA to form double Holliday junction for resynthesis of the missing DNA at the break site (49). Therefore, we analyzed in KU80-GFP-expressing C2C7 myoblasts the local enrichment of γH2AX as DSB marker (47) together with the recruitment of KU80-GFP as NHEJ actor, and RAD51 as HR factor, at different time-points after targeted irradiation with protons or α-particles (Fig. 3).

In myoblasts we first observed a pan-nuclear γH2AX staining appearing 1 h after localized irradiation with 1,000 α-particles and being resolved at later time-points (Fig. 3, A). These results are consistent with previous published studies using charged particle irradiation (50,51). Furthermore, this pan nuclear signal decreases as the number of delivered particles diminishes and is visible as soon as the number of delivered α-particles reaches 200 (Fig. 3, A). Despite that, to avoid introducing a bias in the quantification of fluorescence signal intensity, we analyzed the whole nuclear γH2AX signal at different time-points after localized irradiation. Accordingly, at each time-point we clearly observed a reduction in the γH2AX signal as a function of the dose (Fig. 3, B), directly correlating with a decrease in the number of particles delivered, from 1,000 to 50 α-particles, and with the time elapsed after micro-irradiation, from 1 to 6 h, suggesting the ongoing DSB repair. To confirm the correlation of γH2AX fluorescence intensity with the amount of DNA damage induced by a number of particles targeted, we also assessed the total nuclear γH2AX signal in the C2C7 cells irradiated with intermediate number of α-particles (i.e., 500 and 100 α-particles) (Fig. S3, A). One-hour post-irradiation, we found that the γH2AX signal is indeed the highest after 1,000 α-particles irradiation and it significantly and continuously decreases in a correlated manner with the reduction of the number of particles delivered, from 500 to 50 α-particles (Fig. S3, A).

Within the first 10 minutes after irradiation with 1,000 α-particles the KU80-GFP signal induced at the irradiation site is 5- and 10-fold higher than that induced by a micro-irradiation with 200 and 50 α-particles, respectively. Afterwards, the intensity of KU80-GFP signal (Fig. 3, C-D) decreases with a similar pattern to that of γH2AX (Fig. 3, B-C). Six hours post 1,000 α-particle irradiation, we observed a clear decrease in KU80-GFP signal at localized DNA damage site. However, the fluorescence signal intensity detected after irradiation with lower number of particles (i.e., 200 and 50 α-particles) at the irradiation site was too weak (under our technical imaging conditions) to distinguish a difference 1 h post-irradiation (Fig. 3, C-D and Fig. S3, B). Contrary to KU80-GFP, upon irradiation with 1,000 α-particles the RAD51 fluorescence intensity at the localized irradiation site remains relatively low 10 min and 1 h post-irradiation (Fig. 3, C-E). Interestingly, decreasing the number of α-particles from 1,000 to

50 led to an increase in the RAD51 signal intensity at the localized irradiation site, inversely correlating with the KU80-GFP signal and the number of particles delivered (Fig. S3, B).

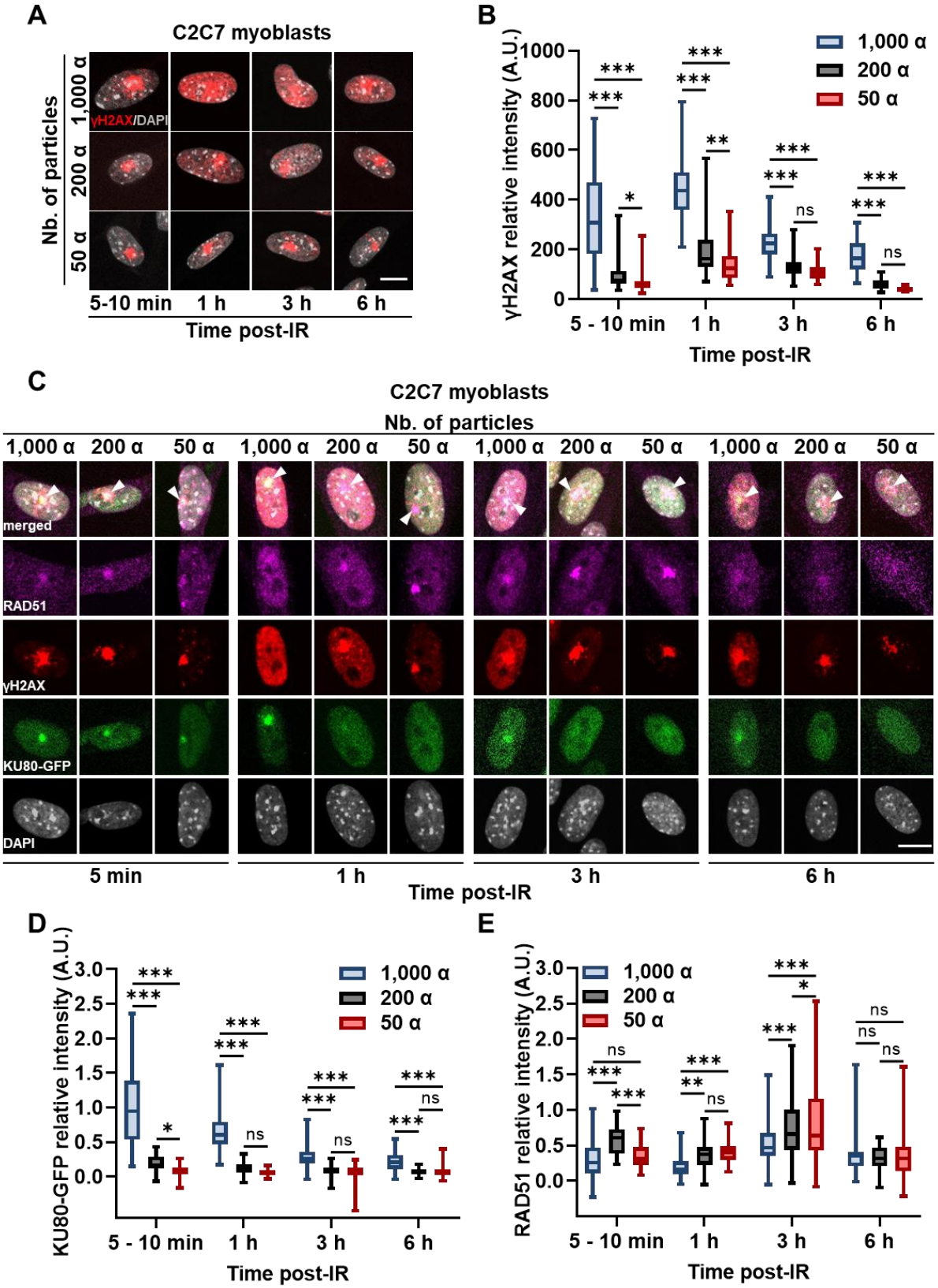

Figure 3: DSB repair mechanisms taking role in myoblasts upon α-particle micro-irradiation with reducing number of particles. (A) *Representative images of nuclear γH2AX pattern at the indicated time-points upon micro-irradiation with 1,000, 200 and 50 α-particles in stably KU80-GFP-expressing*

C2C7 myoblasts immunolabelled against γH2AX. DNA counterstained with DAPI. Scale bar, 10 µm. ***(B)*** *Mean nuclear fluorescence intensities of γH2AX within nuclei of cells from (A) at indicated time-points upon micro-irradiation with the indicated α-particle number. N= 3 independent experiments with 50 - 177 cells / condition analyzed.* ***(C)*** *Representative images of stably KU80-GFP-expressing myoblasts immunolabelled against the HR factor RAD51 and γH2AX at the indicated time-points upon irradiation with the indicated number of α-particles. Localized irradiation site with white arrowhead. DNA counterstained with DAPI. Scale bar, 10 µm.* ***(D, E)*** *Mean fluorescence intensities of recruited KU80-GFP (D), and immunostaining with anti-RAD51 antibody (E) at the indicated time-points after micro-irradiation with the indicated number of α-particles. N= 3 independent experiments, with 51 - 164 cells / condition analyzed. In the box-plots, boxes represent the median with upper and lower quartiles and whiskers represent the min and max values. Significance by 2-way ANOVA with post-hoc Tukey's multiple comparison test against the number of α-particles at each indicated time-points. The p-value are ns p> 0,05, * p< 0.05, ** p< 0.01, *** p< 0.001.*

In addition, in all of the irradiations with α-particles (1,000; 200 or 50 α-particles), the RAD51 signal reaches a maximum, with a fluorescence level 2 folds higher for each condition, 3 h post- irradiation, and then diminishes at the time-point 6 h post-irradiation (Fig. 3, C and E). Additionally, in order to summarize the results obtained in Figures 3 and S3, we performed partial least squares-discriminant analysis (PLS-DA) (Fig. S4, A-B) by taking advantage of measured fluorescence intensities of RAD51 and KU80-GFP at the irradiation sites and of nuclear γH2AX for each individual cell. With these cellular identities, PLS-DA adequately classified the cell groups depending on the active DSBR mechanisms (RAD51, KU80-GFP intensities) and dynamics (γH2AX) upon irradiation with different number of α-particles (Fig. S4, A) and throughout time post-irradiation (Fig. S4, B). Altogether, our data confirmed that in myoblasts NHEJ is the principal pathway involved in the repair of DSBs induced by α-particles irradiation. However, HR plays an important role at the late DSBR stages, in agreement with a potential switch of DSBR pathways from NHEJ to HR as described in (52). Surprisingly, upon local irradiations with low number of α-particles, implication of HR seems to be sooner, in the early stages of DSBR than irradiation by 1,000 α-particles.

As we have just observed differences in DSBR mechanisms and dynamics by reducing energy deposition of α-particles, thereby reducing the amount of induced DNA damage, we decided to investigate and compare the DDR of myoblasts to DNA damage of different complexities by using protons. Therefore, we analyzed the fluorescence intensities of RAD51 and KU80-GFP at the local irradiation sites as well as nuclear γH2AX signal 5 min to 6 h post-irradiation with 10,000 protons and 1,000 α-particles, leading to similar energy depositions. Upon localized proton irradiation of myoblasts, RAD51 fluorescence intensity reaches its maximum at 1 h post-irradiation, sooner than upon micro-irradiation with α-particles (Fig 4, A). Moreover, the decrease in RAD51 signal at the localized irradiation site is faster upon proton irradiation, starting from 3 h post-irradiation (Fig. 4, A). However, the KU80-GFP recruitment and release kinetics at local DNA damage sites are similar to those observed in myoblasts irradiated with α-particles, but on a smaller scale (Fig. 4, B). Altogether, the faster release of RAD51 and the lower amount of KU80-GFP at the local DNA damage site upon micro-irradiation with 10,000 protons, in comparison to micro-irradiation with 1,000 α-particles (Fig.4, A-B), also in agreement with the faster disappearance of γH2AX signal over time after IR (Fig. 4, C), suggest a faster repair of DNA lesions induced by proton micro-irradiation. Accordingly, the addition of the data obtained in Figure 4 to the previous PLS-DA analysis (Fig. S4, A-B) showed distinct scatterplot projections of myoblasts micro-irradiated by protons or α-particles both for the 1 h and 3 h time-points due to strong differences of both KU80-GFP and RAD51 fluorescence identities of cell groups (Fig. S4, C-D). The results obtained from PLS-DA analysis reinforce the implication on the diversity of DNA damage repair dynamics and mechanisms upon irradiation with different particles.

Since we observed that HR seems to be involved sooner in the process of proton-induced DNA damage repair than that induced by α-particles, we analyzed the behavior of the heterochromatin protein 1 isoform, HP1α. It was previously reported that HP1α recruited by p150CAF-1, the largest subunit of histone chaperone chromatin assembly factor 1 (CAF-1), to the site of DNA damage induced by laser micro-irradiation promotes HR (53). Thus, to further characterize the cellular response to IR, we analyzed the recruitment kinetics of HP1α within stably HP1α-GFP-expressing C2C7 myoblasts upon localized irradiation with 10,000 protons or 1,000 α-particles (Fig. 4, Di). In agreement with our data

above (Fig. 4, A), HP1α-GFP recruitment to localized irradiation site is also higher upon proton irradiation than upon α-particle irradiation (Fig. 4, Dii). These results suggest that HR-mediated DSBR takes place earlier upon proton micro-irradiation when compared to α-particle one.

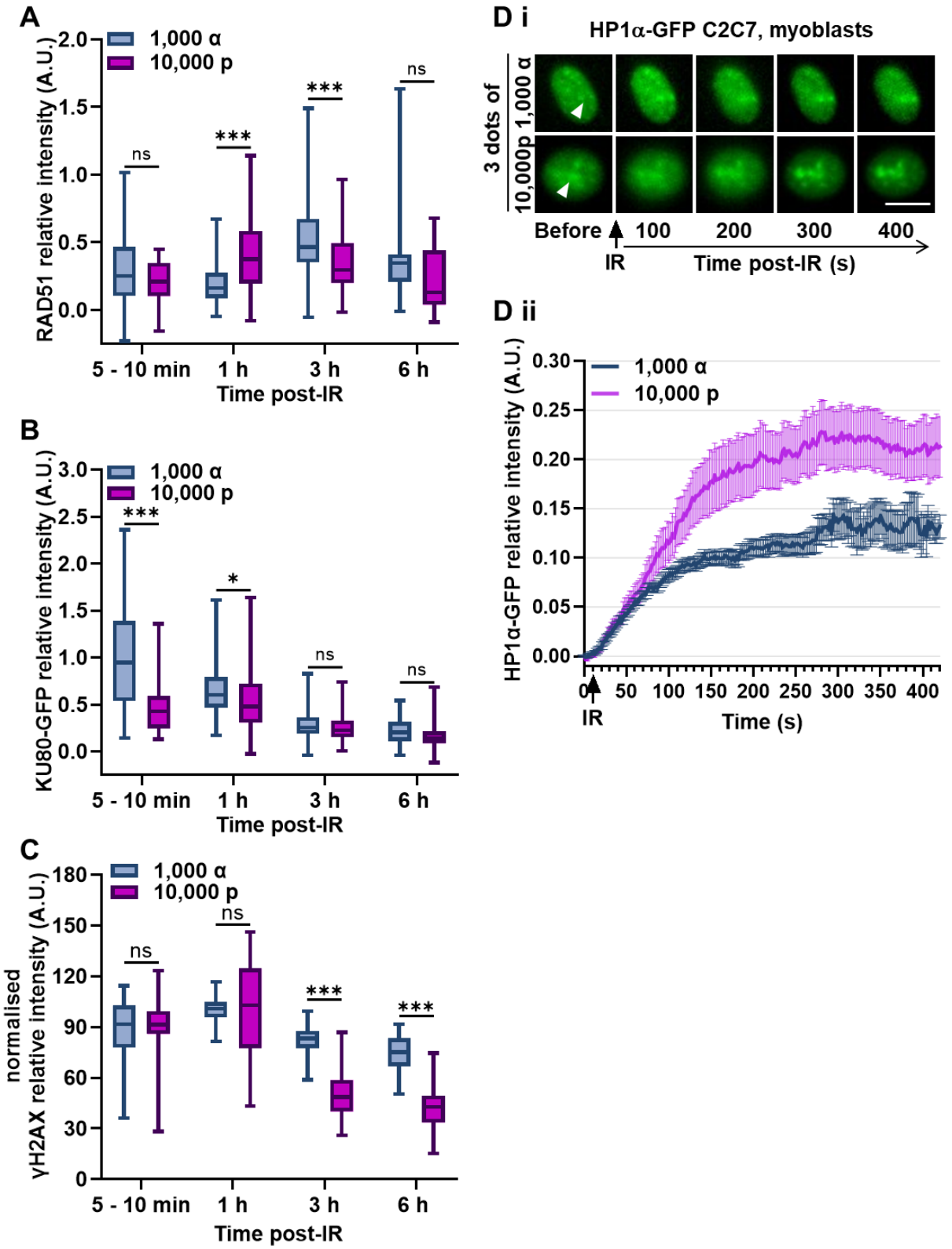

Figure 4: DSB repair upon α-particle and proton irradiation. (A -C) *Mean fluorescence intensities of recruited immunolabelled RAD51 (A), recruited KU80-GFP (B) and immunolabelled total nuclear γH2AX (C) at indicated time-points upon α-particle and proton irradiation. N= 3 independent experiments, with*

*55 – 177 cells / condition analyzed. The data are presented in box-plots. Significance by 2-way ANOVA with post-hoc Sidak's comparison test against the number of particles delivered at each indicated time-points. The p-value are ns p> 0,05, * p< 0.05, ** p< 0.01, *** p< 0.001.* ***(D)*** *Representative images (Di) and kinetic curves (Dii) of HP1α-GFP recruitment in C2C7 myoblasts upon 1,000 α-particles and 10,000 protons micro-irradiation. N= 3 independent experiments, mean ± SEM from 30 - 39 cells / condition analyzed.*

Here we showed that in myoblasts NHEJ is the initial and principal repair pathway to process DNA damage induced by α-particles micro-irradiation and then there is a switch of repair machinery to HR around 3 h post-irradiation. Additionally, decreasing the number of α-particles delivered also favors repair of IR-induced DNA damage by HR. Upon proton irradiation, unlike α-particle-induced DNA damage, both NHEJ and HR seems to be actively involved in the initial stages of DNA damage processing, and at a faster pace.

Discussion

Along with increasing cancer survival rates, the late side effects of radiotherapy treatments on muscle tissue are becoming more apparent (16-18). Muscle is one of healthy neighboring tissue majorly exposed during IR treatment leading to impaired life quality of cancer patients. This is reported to be more severe in pediatric patients who still have an ongoing muscle development (54) and thus their muscle tissue includes all forms of myogenic cells: quiescent, active muscle stem cells; cycling and differentiating precursor cells, myoblasts; and post-mitotic myofibers, as was reported in mice (29). Previously we have shown that myotubes have reduced DNA damage response (DDR) upon irradiation and slower DSB repair capacity in comparison to their precursor cells, myoblasts (33). However, the repair mechanisms acting in proliferating myoblasts remained poorly characterized. Therefore, to understand why cancer patients suffer from musculoskeletal disorders, and especially why pediatric cancer patients have more severe side effects upon radiotherapy, we investigated the DDR in myogenic cells upon irradiation with different types of charged particles by using ion microbeam technology (38), offering the advantage of delivering controlled number of particles within a sub-nuclear region of cell nucleus. Thereby, we were able to monitor the cellular response to the locally induced DNA damage, particularly by ionizing radiation, while most of the published local DNA damage studies are performed by laser micro-irradiation.

Dose-dependent retention of KU80 at DNA damage site.

We found here that the level of KU80 recruited and retained at the local damage site directly correlates with the number of particles delivered within the nuclei of myoblasts, indicating that NHEJ-mediated DSB repair can handle increasing amounts of lesions.

Additionally, in all conditions while myotubes show lower recruitment of KU80 to localized irradiation site in comparison to myoblasts, strengthening the data of our previous work (33), KU80 in myotubes is retained longer on damaged DNA. One reason for the longer persistence of KU80 at local DNA damage sites in myotubes could be due to the absence of HR repair pathway, as reported in (32,33), leaving myotubes entirely dependent on NHEJ to repair IR-induced DSBs, whereas cycling myoblasts still have the capability of deploying HR.

Finally, as previously reported, the recruitment of KU80 occurs in all myogenic cells and its release from DNA may happen when HR takes place to mediate repair of more complex DSBs (52,55). Thus, the shorter retention of KU80 upon irradiation with smaller number of particles could be either due to generation of smaller number of DSBs, or due to the nature of the lesions requiring a potentially earlier switch of DSBR mechanism from NHEJ to HR when NHEJ is not sufficient to cope with the complexity of IR-induced DNA lesions.

Recruitment of 53BP1 correlates with the presence of HR activity in myogenic cells.

53BP1 is a crucial DDR protein, which has multiple roles in DSBR (56). The recruitment of 53BP1 to DSBs in proliferative cells promotes DSBR through NHEJ by restricting the 5' DNA end resection and thus preventing the implementation of DSBR mediated by HR (45,46). We showed here that 53BP1

recruitment is very low or even almost non-existent at the charged particle irradiation sites in post-mitotic myotubes. This reduced 53BP1 recruitment in myotubes could be the consequence of a general decline in NHEJ along myogenic differentiation, as found above with KU80 (33). However, we can also hypothesize that in absence of functional HR in myotubes (33), 53BP1 is not required, since there is no need to counteract HR implementation to promote NHEJ. Indeed, NHEJ can efficiently occur in absence of 53BP1 for most DSBs (57). However, besides its role in the choice of DNA repair pathway, 53BP1 recruitment also induces the chromatin relaxation for the ATM-dependent slow-kinetic DSBR at heterochromatin regions (58). Interestingly, it was reported that in myotubes the activity of ATM and its downstream effectors is low (59), which would leave the DNA lesions in heterochromatin regions unprocessed or difficult to process. Accordingly, our observations suggest that the very late recruitment of 53BP1 at 6 h post-irradiation would probably provide a protection to unprocessed broken DNA ends, which was reported to be an ATM-independent mechanism (60). Likewise, although in myoblasts 53BP1 accumulation at DNA damage sites is already higher than in myotubes at the early time-points upon micro-irradiation, it also reaches to its maximum at the later time-points when KU80 becomes undetectable.

Low and delayed recruitment of 53BP1 upon micro-irradiation with high number of charged particles suggests that 53BP1 is potentially dispensable at early stages of DSBR in myogenic cells but it is required at the later stages for the processing of more complex DSBs. However, we have also noticed that 53BP1 accumulation is higher when cells are micro-irradiated with a smaller number of particles, either proton or α-particle. Concurrently, this was also the case with RAD51, suggesting earlier commitment of HR. Recently, sooner implication of HR was also reported in lymphoblastoid cell lines upon exposure to low doses of X-ray irradiation (61). Moreover, RAD51 recruitment has also been correlated with 53BP1 foci formation in human lung epithelial carcinoma A549 cells upon low doses of X-ray irradiation (62). Besides, in the absence of p150CAF-1-dependent HP1α recruitment, HR was found to be suppressed as well as the recruitment of 53BP1 to laser micro-irradiation-induced DNA damage sites (53). Hence, in agreement with the literature, the direct correlation of RAD51 and 53BP1 recruitment to locally damaged DNA sites upon irradiation with low number of charged particle could implicate 53BP1 in the DNA broken end protection from extensive resection, limiting alternative DSBR pathways (i.e., single strand annealing, SSA, or alternative non-homologous end-joining, alt-NHEJ) (63), and allowing the HR to take over. Indeed, upon localized irradiation with high particle number, unlike strong accumulation of KU80 favoring NHEJ, RAD51 accumulation is delayed to later stages, most likely to process remaining unrepaired DNA broken ends by HR. This could also explain the slow and delayed accumulation of 53BP1 upon micro-irradiation with high number of particles, to protect the unrepaired broken DNA ends until being processed by HR. Thus, although it is contradictory to its generic role in favoring NHEJ, our data imply a novel role for 53BP1 in broken DNA end protection, if not favoring, at least to maintain the DNA ends to be processed by HR. In agreement with this, the unexpected behavior of 53BP1 in myotubes upon local DNA damage induction states that 53BP1 could be dispensable in NHEJ-dependent DSBR of myogenic cells.

HR is implicated sooner in the processing of DNA lesions induced by protons, which are also repaired faster.

There are multiple studies pointing out that irradiations with different types of particles (i.e., species, energy and linear energy transfer (LET) of particles) induce different kinds of DNA damage (64,65) with different levels of complexity (i.e., different types of DNA lesions in the same DNA region) and clustering (i.e., accumulation of DNA damage in the same DNA region) (66,67). Apart from DNA lesions directly induced by direct interaction with the DNA molecule, ionizing radiation (IR) also creates reactive species (i.e., reactive oxygen or nitrogen species, ROS or RNS) by interacting with other molecules, such as water, proteins, etc… (68-70), which then also contribute to further formation of DNA damage within irradiated cells. Computational approaches (66,67) showed that irradiations with α-particles lead to a small number of DNA damage sites with concentrated clusters of complex DNA lesions compared to irradiations with protons, which give a higher number of DNA damage sites containing less clusters of complex DNA lesions. Here, with the use of the MIRCOM ion microbeam, we induce, whatever the particle delivered, protons or α-particles, DNA lesions within a very localized subnuclear area, thus potentially more clustered.

Accordingly, we do detect histone H2AX phosphorylation (γH2AX) only localized at the irradiation sites, suggesting the formation of localized irradiation-induced DSBs. However, after delivering at least 200 α-particles we also observe that H2AX phosphorylation propagates transiently throughout the whole cell nucleus, in addition to a persistent γH2AX signal at the irradiation sites up to 6 h post-irradiation. In agreement with our previous findings (33) and the literature (50,51), this pan-nuclear γH2AX signal is not linked to the induction of apoptosis (71) nor to the presence of DSBs, since, like others (50,51), we do not find 53BP1 accumulation outside the localized irradiation sites. This pan-nuclear γH2AX is likely due to a stress signal resulting from an increase in indirect DNA lesions induced by reactive species, and/or increase in the complexity or clustering of DNA damage generated by charged particle-irradiation (50,51,64,70). Nevertheless, although this γH2AX signal does not correspond to high LET IR-induced DSBs, it still directly correlates with the number of charged particles delivered during irradiation and its disappearance with the repair of DNA lesions induced by protons or α-particles. Based on our results, we can hypothesize that the pan-nuclear γH2AX signal could serve as a marker of increased complexity and/or clustering of IR-induced DNA lesions, as long as it does not coincide with the induction of apoptosis. Finally, regardless to the type of charged particle, the robust recruitment and the quick release of KU80-GFP at irradiation sites with low number of α-particles or protons suggest that the easy-to-ligate DNA broken-ends are quickly processed by NHEJ. Then, HR processes the remaining complex DNA lesions, with a sooner implication when irradiation is performed with low number of particles.

Furthermore, the faster disappearance of γH2AX signal after proton irradiation, which we have observed to be concomitant with the faster decrease in KU80-GFP and RAD51 signals at targeted irradiation sites suggest that DNA damage induced by proton is processed faster than the ones induced by α-particle with comparable energy deposition. Our findings agree with simulation studies suggesting that α-particles induce more complex and clustered DNA damage than protons at comparable deposited energies (64). While NHEJ is thought as the principal DNA repair mechanism for DNA damage induced by charged particle-irradiation, the importance of HR was also recently reported upon proton irradiation (72). Besides, our data show an earlier recruitment and disappearance of 53BP1 upon proton irradiation, in addition to a higher recruitment of HR-promoting factor HP1α, in comparison to α-particle-irradiation in myoblasts. Thus, we confirm that HR is actively involved in the proton-induced DNA damage processing alongside with NHEJ, while it takes place at the later stages upon α-particle irradiation. These results suggest that DNA damage induced by α-particles would require more DNA end-processing by NHEJ before leaving to HR the repair of the remaining DSBs, leading to a slower resolution of the γH2AX signal. Moreover, a faster DSBR component in myoblasts, despite lower recruitment of KU80-GFP to the DNA damage site upon irradiation with protons than with α-particles also supports our hypothesis that while α-particles induced DSBR relays on mainly on NHEJ, proton induced DNA damage is processed by more than one mechanism, notably by HR. This could also explain the longer persistence of KU80-GFP at the DNA damage site in HR-deprived myotubes upon irradiation with protons than with α-particles, probably to compensate the lack of HR activity. In conclusion, in proliferating myoblasts the DSBR mechanism engaged depends not only on the deposited energy (i.e., increased number of charged particles), but also on the type of the charged particle. In general, in myoblasts HR is involved later, potentially to repair unprocessed more complex and/or clustered DNA lesions. However, HR also seems to be more strikingly involved in the repair of DNA damage induced by proton irradiation. Moreover, myogenic cells seem to repair DSBs with distinct mechanisms that adapt and change throughout myogenic differentiation, in which 53BP1 is dispensable in myotubes and in the NHEJ-dependent DSBR of myoblasts. Future studies based on the inactivation of each pathway would provide a better deciphering of the charged particle-induced DNA damage processing.

Finally, while this study provides further understanding on how skeletal muscle cells respond to different radiation qualities that could be used during radiotherapies, it also points out the importance of considering the neighboring healthy tissue in radiotherapy modalities and treatment planification to be performed on patients. This is even more vital when radiotherapy is particularly combined with chemotherapies, targeting certain DNA damage repair mechanisms and cell cycle control. In that matter, these treatments could also block the recovery of the healthy tissue from induced DNA damage, especially in pediatric patients, who are still physiologically growing and for instance hosting actively cycling myogenic cells apart from differentiated skeletal muscle cells, hence multiple DSBR mechanisms.

Author Contributions

HHS: Conceptualization, Data curation, Formal Analysis, Investigation, Methodology, Project administration, Validation, Visualization, Writing – original draft. **ATJ:** Investigation, Methodology. **MCM:** Methodology (α-particle and proton irradiation experiments). **FV:** Methodology, Supervision (α-particle and proton irradiation experiments). **MAB:** Formal Analysis. **MB:** Supervision, Validation. **CB:** Formal analysis, Funding acquisition, Project administration, Supervision, Validation, Visualization, Writing – original draft.

All authors read and approved the final manuscript.

Acknowledgments

The authors thank the PSE-SANTE/SDOS/LMDN team of the IRSN for their excellent technical expertise on the MIRCOM facility and Valérie Buard (PSE-SANTE/SERAMED/LRMed) for her technical support on the IRSN confocal microscopy facility. The authors are grateful to P. Radicella for his critical reading of the manuscript, and to G. Gruel for his helpful suggestions.

Funding

This work was supported by Institute National du Cancer, France (Grant number: PLBIO19-126 LS194750 INCa 2019).

Data Availability Statement

The source data for the main and supplemental figures are available in the published article and its online supplemental files.

Conflict of Interest Statement

The authors declare that they have no conflict of interest.

References

1. Wang, J.J., Lei, K.F. and Han, F. (2018) Tumor microenvironment: recent advances in various cancer treatments. *Eur Rev Med Pharmacol Sci*, **22**, 3855-3864.
2. Han, W. and Yu, K.N. (2009), *Advances in Biomedical Sciences and Engineering*, pp. 204-262. doi: 10.2174/97816080504061090101020 4.
3. Maier, P., Hartmann, L., Wenz, F. and Herskind, C. (2016) Cellular Pathways in Response to Ionizing Radiation and Their Targetability for Tumor Radiosensitization. *International journal of molecular sciences*, **17**. doi: 10.3390/ijms17010102.
4. Zhao, L., Bao, C., Shang, Y., He, X., Ma, C., Lei, X., Mi, D. and Sun, Y. (2020) The Determinant of DNA Repair Pathway Choices in Ionising Radiation-Induced DNA Double-Strand Breaks. *BioMed research international*, **2020**, 4834965. doi: 10.1155/2020/4834965.
5. van de Kamp, G., Heemskerk, T., Kanaar, R. and Essers, J. (2021) DNA Double Strand Break Repair Pathways in Response to Different Types of Ionizing Radiation. *Front Genet*, **12**.
6. Beucher, A., Birraux, J., Tchouandong, L., Barton, O., Shibata, A., Conrad, S., Goodarzi, A.A., Krempler, A., Jeggo, P.A. and Löbrich, M. (2009) ATM and Artemis promote homologous recombination of radiation-induced DNA double-strand breaks in G2. *The EMBO journal*, **28**, 3413-3427. doi: 10.1038/emboj.2009.276.
7. Nick McElhinny, S.A., Snowden, C.M., McCarville, J. and Ramsden, D.A. (2000) Ku recruits the XRCC4-ligase IV complex to DNA ends. *Molecular and cellular biology*, **20**, 2996-3003. doi: 10.1128/mcb.20.9.2996-3003.2000.
8. Ahnesorg, P., Smith, P. and Jackson, S.P. (2006) XLF interacts with the XRCC4-DNA ligase IV complex to promote DNA nonhomologous end-joining. *Cell*, **124**, 301-313. doi: 10.1016/j.cell.2005.12.031.
9. Grosse, N., Fontana, A.O., Hug, E.B., Lomax, A., Coray, A., Augsburger, M., Paganetti, H., Sartori, A.A. and Pruschy, M. (2014) Deficiency in homologous recombination renders Mammalian cells more sensitive to proton versus photon irradiation. *International journal of radiation oncology, biology, physics*, **88**, 175-181. doi: 10.1016/j.ijrobp.2013.09.041.

10. Gerelchuluun, A., Manabe, E., Ishikawa, T., Sun, L., Itoh, K., Sakae, T., Suzuki, K., Hirayama, R., Asaithamby, A., Chen, D.J. and Tsuboi, K. (2015) The major DNA repair pathway after both proton and carbon-ion radiation is NHEJ, but the HR pathway is more relevant in carbon ions. *Radiation research*, **183**, 345-356. doi: 10.1667/rr13904.1.
11. Bright, S.J., Flint, D.B., Chakraborty, S., McFadden, C.H., Yoon, D.S., Bronk, L., Titt, U., Mohan, R., Grosshans, D.R., Sumazin, P. *et al.* (2019) Nonhomologous End Joining Is More Important Than Proton Linear Energy Transfer in Dictating Cell Death. *International journal of radiation oncology, biology, physics*, **105**, 1119-1125.
12. Hua, C., Gray, J.M., Merchant, T.E., Kun, L.E. and Krasin, M.J. (2008) Treatment planning and delivery of external beam radiotherapy for pediatric sarcoma: the St. Jude Children's Research Hospital experience. *International journal of radiation oncology, biology, physics*, **70**, 1598-1606. doi: 10.1016/j.ijrobp.2007.12.013.
13. Nahum, A.E. (2015) The radiobiology of hypofractionation. *Clinical oncology (Royal College of Radiologists (Great Britain))*, **27**, 260-269. doi: 10.1016/j.clon.2015.02.001.
14. Hannan, R., Christensen, M., Christie, A., Garant, A., Pedrosa, I., Robles, L., Mannala, S., Wang, C., Hammers, H., Arafat, W. *et al.* (2022) Stereotactic Ablative Radiation for Systemic Therapy-naïve Oligometastatic Kidney Cancer. *European urology oncology*, **5**, 695-703. doi: 10.1016/j.euo.2022.06.008.
15. Iturri, L., Bertho, A., Lamirault, C., Juchaux, M., Gilbert, C., Espenon, J., Sebrie, C., Jourdain, L., Pouzoulet, F., Verrelle, P. *et al.* (2023) Proton FLASH Radiation Therapy and Immune Infiltration: Evaluation in an Orthotopic Glioma Rat Model. *International journal of radiation oncology, biology, physics*, **116**, 655-665.
16. Siegel, R.L., Miller, K.D. and Jemal, A. (2020) Cancer statistics, 2020. *CA: a cancer journal for clinicians*, **70**, 7-30. doi: 10.3322/caac.21590.
17. Zhang, L.L., Mao, Y.P., Zhou, G.Q., Tang, L.L., Qi, Z.Y., Lin, L., Yao, J.J., Ma, J., Lin, A.H. and Sun, Y. (2015) The Evolution of and Risk Factors for Neck Muscle Atrophy and Weakness in Nasopharyngeal Carcinoma Treated With Intensity-Modulated Radiotherapy: A Retrospective Study in an Endemic Area. *Medicine*, **94**, e1294. doi: 10.1097/md.0000000000001294.
18. Paulino, A.C. (2004) Late effects of radiotherapy for pediatric extremity sarcomas. *International journal of radiation oncology, biology, physics*, **60**, 265-274. doi: 10.1016/j.ijrobp.2004.02.001.
19. Frontera, W.R. and Ochala, J. (2015) Skeletal muscle: a brief review of structure and function. *Calcified tissue international*, **96**, 183-195. doi: 10.1007/s00223-014-9915-y.
20. Gillette, E.L., Mahler, P.A., Powers, B.E., Gillette, S.M. and Vujaskovic, Z. (1995) Late radiation injury to muscle and peripheral nerves. *International journal of radiation oncology, biology, physics*, **31**, 1309-1318. doi: 10.1016/0360-3016(94)00422-h.
21. Coquard, R. (1997) [Late effects of radiotherapy on the skeletal muscle]. *Cancer Radiother*, **1**, 790-791.
22. Olivé, M., Blanco, R., Rivera, R., Cinos, C. and Ferrer, I. (1995) Cell death induced by gamma irradiation of developing skeletal muscle. *Journal of anatomy*, **187 (Pt 1)**, 127-132.
23. Cui, W., Bennett, A.W., Zhang, P., Barrow, K.R., Kearney, S.R., Hankey, K.G., Taylor-Howell, C., Gibbs, A.M., Smith, C.P. and MacVittie, T.J. (2016) A non-human primate model of radiation-induced cachexia. *Sci Rep*, **6**, 23612. doi: 10.1038/srep23612.
24. D'Souza, D., Roubos, S., Larkin, J., Lloyd, J., Emmons, R., Chen, H. and De Lisio, M. (2019) The Late Effects of Radiation Therapy on Skeletal Muscle Morphology and Progenitor Cell Content are Influenced by Diet-Induced Obesity and Exercise Training in Male Mice. *Sci Rep*, **9**, 019-43204.
25. Paris, N.D., Kallenbach, J.G., Bachman, J.F., Blanc, R.S., Johnston, C.J., Hernady, E., Williams, J.P. and Chakkalakal, J.V. (2020) Chemoradiation impairs myofiber hypertrophic growth in a pediatric tumor model. *Sci Rep*, **10**, 020-75913.
26. Kallenbach, J.G., Bachman, J.F., Paris, N.D., Blanc, R.S., O'Connor, T., Furati, E., Williams, J.P. and Chakkalakal, J.V. (2022) Muscle-specific functional deficits and lifelong fibrosis in response to paediatric radiotherapy and tumour elimination. *Journal of cachexia, sarcopenia and muscle*, **13**, 296-310. doi: 10.1002/jcsm.12902.
27. O'Connor, T.N., Kallenbach, J.G., Orciuoli, H.M., Paris, N.D., Bachman, J.F., Johnston, C.J., Hernady, E., Williams, J.P., Dirksen, R.T. and Chakkalakal, J.V. (2022) Endurance exercise attenuates juvenile irradiation-induced skeletal muscle functional decline and mitochondrial stress. *Skelet Muscle*, **12**, 022-00291.
28. Seale, P., Asakura, A. and Rudnicki, M.A. (2001) The potential of muscle stem cells. *Developmental cell*, **1**, 333-342. doi: 10.1016/s1534-5807(01)00049-1.

29. Gattazzo, F., Laurent, B., Relaix, F., Rouard, H. and Didier, N. (2020) Distinct Phases of Postnatal Skeletal Muscle Growth Govern the Progressive Establishment of Muscle Stem Cell Quiescence. *Stem cell reports*, **15**, 597-611. doi: 10.1016/j.stemcr.2020.07.011.
30. Tajbakhsh, S. (2009) Skeletal muscle stem cells in developmental versus regenerative myogenesis. *Journal of internal medicine*, **266**, 372-389. doi: 10.1111/j.1365-2796.2009.02158.x.
31. Collins, C.A., Olsen, I., Zammit, P.S., Heslop, L., Petrie, A., Partridge, T.A. and Morgan, J.E. (2005) Stem cell function, self-renewal, and behavioral heterogeneity of cells from the adult muscle satellite cell niche. *Cell*, **122**, 289-301. doi: 10.1016/j.cell.2005.05.010.
32. Vahidi Ferdousi, L., Rocheteau, P., Chayot, R., Montagne, B., Chaker, Z., Flamant, P., Tajbakhsh, S. and Ricchetti, M. (2014) More efficient repair of DNA double-strand breaks in skeletal muscle stem cells compared to their committed progeny. *Stem cell research*, **13**, 492-507. doi: 10.1016/j.scr.2014.08.005.
33. Sutcu, H.H., Rassinoux, P., Donnio, L.M., Neuillet, D., Vianna, F., Gabillot, O., Mari, P.O., Baldeyron, C. and Giglia-Mari, G. (2024) Decline of DNA damage response along with myogenic differentiation. *Life science alliance*, **7**. doi: 10.26508/lsa.202302279.
34. Sutcu, H.H., Montagne, B. and Ricchetti, M. (2023) DNA-PKcs regulates myogenesis in an Akt-dependent manner independent of induced DNA damage. *Cell death and differentiation*, **30**, 1900-1915. doi: 10.1038/s41418-023-01177-2.
35. Barberet, P. and Seznec, H. (2015) Advances in microbeam technologies and applications to radiation biology. *Radiation protection dosimetry*, **166**, 182-187. doi: 10.1093/rpd/ncv192.
36. Pinset, C., Montarras, D., Chenevert, J., Minty, A., Barton, P., Laurent, C. and Gros, F. (1988) Control of myogenesis in the mouse myogenic C2 cell line by medium composition and by insulin: characterization of permissive and inducible C2 myoblasts. *Differentiation; research in biological diversity*, **38**, 28-34. doi: 10.1111/j.1432-0436.1988.tb00588.x.
37. Bourret, S., Vianna, F., Devès, G., Atallah, V., Moretto, P., Seznec, H. and Barberet, P. (2014) Fluorescence time-lapse imaging of single cells targeted with a focused scanning charged-particle microbeam. *Nuclear Instruments and Methods in Physics Research, Section B: Beam Interactions with Materials and Atoms*, **325**, 27-34. doi: 10.1016/j.nimb.2014.02.004.
38. Vianna, F., Gonon, G., Lalanne, K., Adam-Guillermin, C., Bottollier-Depois, J.-F., Daudin, L., Dugué, D., Moretto, P., Petit, M., Serani, L. *et al.* (2022) Characterization of MIRCOM, IRSN's new ion microbeam dedicated to targeted irradiation of living biological samples. *Nuclear Instruments and Methods in Physics Research Section B: Beam Interactions with Materials and Atoms*, **515**, 20-30. doi: https://doi.org/10.1016/j.nimb.2022.01.007.
39. Bobyk, L., Vianna, F., Martinez, J.S., Gruel, G., Benderitter, M. and Baldeyron, C. (2022) Differential Recruitment of DNA Repair Proteins KU70/80 and RAD51 upon Microbeam Irradiation with α-Particles. *Biology*, **11**. doi: 10.3390/biology11111652.
40. Ziegler, J.F., Ziegler, M.D. and Biersack, J.P. (2010) SRIM – The stopping and range of ions in matter (2010). *Nuclear Instruments and Methods in Physics Research Section B: Beam Interactions with Materials and Atoms*, **268**, 1818-1823. doi: https://doi.org/10.1016/j.nimb.2010.02.091.
41. Schneider, C.A., Rasband, W.S. and Eliceiri, K.W. (2012) NIH Image to ImageJ: 25 years of image analysis. *Nat Methods*, **9**, 671-675. doi: 10.1038/nmeth.2089.
42. Hastie, T. and Tibshirani, R. (1995) Generalized additive models for medical research. *Statistical methods in medical research*, **4**, 187-196. doi: 10.1177/096228029500400302.
43. Robeska, E., Lalanne, K., Vianna, F., Sutcu, H.H., Khobta, A., Busso, D., Radicella, J.P., Campalans, A. and Baldeyron, C. (2023) Targeted nuclear irradiation with a proton microbeam induces oxidative DNA base damage and triggers the recruitment of DNA glycosylases OGG1 and NTH1. *DNA repair*, **133**, 103610. doi: 10.1016/j.dnarep.2023.103610.
44. Mari, P.O., Florea, B.I., Persengiev, S.P., Verkaik, N.S., Brüggenwirth, H.T., Modesti, M., Giglia-Mari, G., Bezstarosti, K., Demmers, J.A., Luider, T.M. *et al.* (2006) Dynamic assembly of end-joining complexes requires interaction between Ku70/80 and XRCC4. *Proceedings of the National Academy of Sciences of the United States of America*, **103**, 18597-18602. doi: 10.1073/pnas.0609061103.
45. Bunting, S.F., Callén, E., Wong, N., Chen, H.T., Polato, F., Gunn, A., Bothmer, A., Feldhahn, N., Fernandez-Capetillo, O., Cao, L. *et al.* (2010) 53BP1 inhibits homologous recombination in Brca1-deficient cells by blocking resection of DNA breaks. *Cell*, **141**, 243-254. doi: 10.1016/j.cell.2010.03.012.
46. Callen, E., Zong, D., Wu, W., Wong, N., Stanlie, A., Ishikawa, M., Pavani, R., Dumitrache, L.C., Byrum, A.K., Mendez-Dorantes, C. *et al.* (2020) 53BP1 Enforces Distinct Pre- and Post-

resection Blocks on Homologous Recombination. *Molecular cell*, **77**, 26-38 e27. doi: 10.1016/j.molcel.2019.09.024.
47. Goodarzi, A.A. and Jeggo, P.A. (2012) Irradiation induced foci (IRIF) as a biomarker for radiosensitivity. *Mutation research*, **736**, 39-47. doi: 10.1016/j.mrfmmm.2011.05.017.
48. Sung, P. and Robberson, D.L. (1995) DNA strand exchange mediated by a RAD51-ssDNA nucleoprotein filament with polarity opposite to that of RecA. *Cell*, **82**, 453-461. doi: 10.1016/0092-8674(95)90434-4.
49. Baumann, P. and West, S.C. (1998) Role of the human RAD51 protein in homologous recombination and double-stranded-break repair. *Trends in biochemical sciences*, **23**, 247-251. doi: 10.1016/s0968-0004(98)01232-8.
50. Horn, S., Brady, D. and Prise, K. (2015) Alpha particles induce pan-nuclear phosphorylation of H2AX in primary human lymphocytes mediated through ATM. *Biochimica et biophysica acta*, **1853**, 2199-2206. doi: 10.1016/j.bbamcr.2015.06.010.
51. Meyer, B., Voss, K.O., Tobias, F., Jakob, B., Durante, M. and Taucher-Scholz, G. (2013) Clustered DNA damage induces pan-nuclear H2AX phosphorylation mediated by ATM and DNA-PK. *Nucleic acids research*, **41**, 6109-6118. doi: 10.1093/nar/gkt304.
52. Shao, Z., Davis, A.J., Fattah, K.R., So, S., Sun, J., Lee, K.J., Harrison, L., Yang, J. and Chen, D.J. (2012) Persistently bound Ku at DNA ends attenuates DNA end resection and homologous recombination. *DNA repair*, **11**, 310-316. doi: 10.1016/j.dnarep.2011.12.007.
53. Baldeyron, C., Soria, G., Roche, D., Cook, A.J. and Almouzni, G. (2011) HP1alpha recruitment to DNA damage by p150CAF-1 promotes homologous recombination repair. *The Journal of cell biology*, **193**, 81-95. doi: 10.1083/jcb.201101030.
54. Goodenough, C.G., Partin, R.E. and Ness, K.K. (2021) Skeletal Muscle and Childhood Cancer: Where are we now and where we go from here. *Aging and cancer*, **2**, 13-35. doi: 10.1002/aac2.12027.
55. Shibata, A., Conrad, S., Birraux, J., Geuting, V., Barton, O., Ismail, A., Kakarougkas, A., Meek, K., Taucher-Scholz, G., Löbrich, M. and Jeggo, P.A. (2011) Factors determining DNA double-strand break repair pathway choice in G2 phase. *The EMBO journal*, **30**, 1079-1092. doi: 10.1038/emboj.2011.27.
56. Shibata, A. and Jeggo, P.A. (2020) Roles for 53BP1 in the repair of radiation-induced DNA double strand breaks. *DNA repair*, **93**, 102915. doi: 10.1016/j.dnarep.2020.102915.
57. Ward, I.M., Reina-San-Martin, B., Olaru, A., Minn, K., Tamada, K., Lau, J.S., Cascalho, M., Chen, L., Nussenzweig, A., Livak, F. *et al.* (2004) 53BP1 is required for class switch recombination. *The Journal of cell biology*, **165**, 459-464. doi: 10.1083/jcb.200403021.
58. Noon, A.T., Shibata, A., Rief, N., Löbrich, M., Stewart, G.S., Jeggo, P.A. and Goodarzi, A.A. (2010) 53BP1-dependent robust localized KAP-1 phosphorylation is essential for heterochromatic DNA double-strand break repair. *Nature cell biology*, **12**, 177-184. doi: 10.1038/ncb2017.
59. Latella, L., Lukas, J., Simone, C., Puri, P.L. and Bartek, J. (2004) Differentiation-induced radioresistance in muscle cells. *Molecular and cellular biology*, **24**, 6350-6361. doi: 10.1128/mcb.24.14.6350-6361.2004.
60. Rybanska-Spaeder, I., Reynolds, T.L., Chou, J., Prakash, M., Jefferson, T., Huso, D.L., Desiderio, S. and Franco, S. (2013) 53BP1 is limiting for NHEJ repair in ATM-deficient model systems that are subjected to oncogenic stress or radiation. *Molecular cancer research : MCR*, **11**, 1223-1234. doi: 10.1158/1541-7786.mcr-13-0252-t.
61. Mladenov, E., Paul-Konietzko, K., Mladenova, V., Stuschke, M. and Iliakis, G. (2022) Increased Gene Targeting in Hyper-Recombinogenic LymphoBlastoid Cell Lines Leaves Unchanged DSB Processing by Homologous Recombination. *International journal of molecular sciences*, **23**. doi: 10.3390/ijms23169180.
62. Mladenov, E., Staudt, C., Soni, A., Murmann-Konda, T., Siemann-Loekes, M. and Iliakis, G. (2020) Strong suppression of gene conversion with increasing DNA double-strand break load delimited by 53BP1 and RAD52. *Nucleic acids research*, **48**, 1905-1924. doi: 10.1093/nar/gkz1167.
63. Bakr, A., Köcher, S., Volquardsen, J., Petersen, C., Borgmann, K., Dikomey, E., Rothkamm, K. and Mansour, W.Y. (2016) Impaired 53BP1/RIF1 DSB mediated end-protection stimulates CtIP-dependent end resection and switches the repair to PARP1-dependent end joining in G1. *Oncotarget*, **7**, 57679-57693.
64. Bertolet, A., Chamseddine, I., Paganetti, H. and Schuemann, J. (2023) The complexity of DNA damage by radiation follows a Gamma distribution: insights from the Microdosimetric Gamma Model. *Frontiers in oncology*, **13**, 1196502. doi: 10.3389/fonc.2023.1196502.

65. dos Santos, M., Clairand, I., Gruel, G., Barquinero, J.F., Incerti, S. and Villagrasa, C. (2014) Influence of chromatin condensation on the numberof direct dsb damages induced by ions studied using a monte carlo code. *Radiation protection dosimetry*, **161**, 469-473. doi: 10.1093/rpd/ncu029.
66. Nikjoo, H., O'Neill, P., Wilson, W.E. and Goodhead, D.T. (2001) Computational approach for determining the spectrum of DNA damage induced by ionizing radiation. *Radiation research*, **156**, 577-583. doi: 10.1667/0033-7587(2001)156[0577:cafdts]2.0.co;2.
67. Rezaee, M. and Adhikary, A. (2024) The Effects of Particle LET and Fluence on the Complexity and Frequency of Clustered DNA Damage. *DNA*, **4**, 34-51. doi: 10.3390/dna4010002.
68. Azzam, E.I., Jay-Gerin, J.P. and Pain, D. (2012) Ionizing radiation-induced metabolic oxidative stress and prolonged cell injury. *Cancer letters*, **327**, 48-60. doi: 10.1016/j.canlet.2011.12.012.
69. Hong, M., Xu, A., Zhou, H., Wu, L., Randers-Pehrson, G., Santella, R.M., Yu, Z. and Hei, T.K. (2010) Mechanism of genotoxicity induced by targeted cytoplasmic irradiation. *British journal of cancer*, **103**, 1263-1268. doi: 10.1038/sj.bjc.6605888.
70. Răileanu, M., Straticiuc, M., Iancu, D.A., Andrei, R.F., Radu, M. and Bacalum, M. (2022) Proton irradiation induced reactive oxygen species promote morphological and functional changes in HepG2 cells. *Journal of structural biology*, **214**, 107919. doi: 10.1016/j.jsb.2022.107919.
71. Cook, P.J., Ju, B.G., Telese, F., Wang, X., Glass, C.K. and Rosenfeld, M.G. (2009) Tyrosine dephosphorylation of H2AX modulates apoptosis and survival decisions. *Nature*, **458**, 591-596. doi: 10.1038/nature07849.
72. Vitti, E.T. and Parsons, J.L. (2019) The Radiobiological Effects of Proton Beam Therapy: Impact on DNA Damage and Repair. *Cancers*, **11**. doi: 10.3390/cancers11070946.